J. Fluid Mech. (2004), *vol.* 514, *pp.* 327–353.
DOI: 10.1017/S0022112004000394 Printed in the United Kingdom

Intrusive gravity currents in two-layer fluids

By BRUCE R. SUTHERLAND, PATRICK J. KYBA AND MORRIS R. FLYNN

Department of Mathematical and Statistical Sciences, University of Alberta, Edmonton, AB, Canada, T6G 2G1

(Received 1 May 2003 and in revised form 10 May 2004)

We investigate the dynamics of a gravity current that propagates along the interface of a two-layer fluid. The results of the well-studied symmetric case are reproduced in which the upper- and lower-layer depth of the ambient are equal and the density of the intrusion is the average density of the ambient. In addition, we present the first detailed examination of asymmetric circumstances in which the density of the intrusion differs from the mean density of the ambient and in which the upper- and lower-layer fluid depths are unequal. The general equations derived by J. Y. Holyer & H. E. Huppert (*J. Fluid Mech.* vol. 100, 1980, pp. 739–767,), which predict the speed and vertical extent of the gravity current head, are re-expressed in a simpler form that employs the Boussinesq approximation. Approximate analytic solutions are determined using perturbation theory. The predictions are compared with the results of laboratory experiments. We find excellent agreement if the density of the gravity current is the average of the upper- and lower-layer densities weighted by the respective depths of the two layers. However, exact theory significantly underpredicts the gravity current speeds if the current density differs from this weighted-mean average. The discrepancy is attributed to the generation of waves that lead and trail the gravity current head. Empirical support for this assertion is provided through an examination of the observed wave characteristics.

1. Introduction

The classical analysis for a gravity current is that for a dense fluid that moves horizontally along a rigid bottom beneath a less dense ambient fluid (Kármán 1940; Benjamin 1968; Simpson & Britter 1979; Härtel, Meiburg & Necker 2000). Such currents are manifest in the atmosphere, for example, as the flow of air in a sea breeze front which intrudes into the relatively warm, and presumably uniform, ambient air over land (Simpson, Mansfield & Milford 1977). Other geophysical and environmental examples have been compiled by Simpson (1997).

A more complicated circumstance occurs when a gravity current propagates into a non-uniform ambient. For example, when a bottom-propagating gravity current intrudes into a two-layer ambient fluid, the current can, under some circumstances, excite internal waves at the interface between the upper- and lower-layer fluids (Rottman & Simpson 1989). These dynamics have been attributed to the creation of Morning Glory, a fast-moving band of clouds that appears typically in early morning hours in late October over North-Western Australia (Clarke, Smith & Reid 1981; Smith, Crook & Roff 1982). The clouds mark the crest of a solitary wave (alternatively referred to as an atmospheric undular bore) which moves along the morning-time atmospheric inversion (Noonan & Smith 1985; Christie 1992; Menhofer *et al.* 1997).

Though Australia's Morning Glory is an oft-cited example of atmospheric nonlinear waves, waves resulting from interactions between storm systems and atmospheric inversions have been observed over Texas (Clarke 1998), Oklahoma (Haase & Smith 1984) and elsewhere.

The dynamics of the waves have been well-studied. However, the mechanism for their generation is not so well understood. The southward-propagating 'Morning Glory' waves are believed to be created by the interaction with the inversion of synoptic weather systems north of the Gulf of Carpentaria (Clarke 1984; Noonan & Smith 1986). One way that the waves can be generated is through the release of relatively dense cold air that propagates underneath the inversion (Rottman & Simpson 1989). However, another mechanism exists: the synoptic weather system can mix air above and below the inversion and so create a gravity current that propagates along the interface of the inversion rather than underneath it. Indeed, this is the likely mechanism for the generation of northward-propagating 'Morning Glory' waves, which are believed to be created by convective mixing of the atmospheric inversion which overlies Australia's desert interior.

It is not the purpose of this paper to assess the mechanism for 'Morning Glory' waves in realistic atmospheric conditions. Rather, these phenomena are described as motivation for studying the more general and fundamental dynamics of gravity currents that propagate along a density interface. Through laboratory experiments, we will show that interfacial gravity currents, like bottom-propagating currents, can act as a source of nonlinear waves.

We perform a series of lock-release experiments and analyse digitized images of the results to determine the characteristics of the gravity current and waves. The procedure is similar to lock-release experiments of bottom-propagating currents in which dense fluid lock is released into a less dense ambient by the rapid vertical extraction of a gate separating the two fluids (Keulegan 1957; Rottman & Simpson 1983; Hacker, Linden & Dalziel 1996).

The set-up of our experiments and the resulting waves and currents are shown in figure 1. Initially, a gate separates lock-fluid of density ρ_ℓ and a two-layer ambient fluid with upper- and lower-layer fluid densities ρ_0 and ρ_1, respectively (figure 1*a*). In order to ensure the gravity current moves along the interface, we require, $\rho_0 < \rho_\ell < \rho_1$. Upon extraction of the gate, the gravity current moves forward and return flows above and below the current propagate backwards into the lock (figure 1*b*). When the return flows encounter the end of the lock, they reflect and in certain cases (Rottman & Simpson 1983) may generate internal bores that propagate back toward the head of the gravity current moving along the interfaces above and below its tail (figure 1*c*). Meanwhile, the gravity current may excite interfacial waves that lead the current head. Depending on the relative density differences and the depths of the upper- and lower-layer fluids, the leading wave may be either linear or nonlinear.

Previous experiments on interfacial gravity currents have studied the doubly symmetric case in which the upper- and lower-layer fluid depths are equal and the density of the lock fluid is the average density of the ambient (Britter & Simpson 1981; Rooij, Linden & Dalziel 1999; Lowe, Linden & Rottman 2002). In particular, Mehta, Sutherland & Kyba (2002) studied how the evolution of a gravity current changes as it propagates in a two- and three-layer fluid, the latter being established through repeatedly releasing intrusions. They showed that the gravity current propagates steadily in a two-layer fluid, but that it stops propagating in a three-layer fluid as a consequence of depositing its momentum to trailing sinusoidal internal waves and leading double-humped solitary waves.

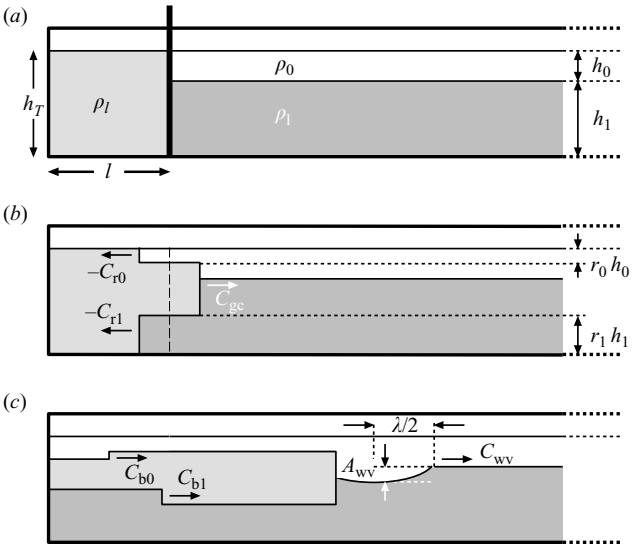

FIGURE 1. Set-up and definition of parameters for intrusion experiments. In (*a*) the fluid in the lock has density ρ_ℓ satisfying $\rho_0 < \rho_\ell < \rho_1$. In (*b*) the gate is extracted and the intrusion propagates to the right while return flows above and below the intrusion propagate to the left. In (*c*) the return flow reflects from the end-wall of the tank leading to the generation of an upper and lower rear-bore that propagate to the right.

The speed of a doubly symmetric gravity current in two layer fluid was examined by de Rooij *et al.* (1999). The experimental results were compared with two theoretical predictions: one extends the results of Benjamin (1968) to an infinitely deep two-layer fluid; the other takes the more general finite-depth predictions of Holyer & Huppert (1980) applied to the doubly-symmetric case.

A central goal of this paper is to run experiments in asymmetric cases and to compare the results with those predicted by Holyer & Huppert (1980). Like the one-layer energy-conserving theory of Benjamin (1968), their theory assumed the system to be in steady state and it required mass and momentum conservation together with Bernoulli's principle to predict the speeds of the gravity current and the return flows above and below the current head. The relative depths of each of the two-layers in the ambient is arbitrary and the density of the interfacial gravity current holds any value between those of the upper and lower layers. (Their theory separately predicts the speed of a bottom-propagating current in a two-layer ambient, but these results are not relevant to the experiments we report upon here.)

Quite generally, their theory is non-Boussinesq in that it allows for significant change in density between the two-layers in the ambient and the current. Here, we recast their formulae in Boussinesq form, which is appropriate for comparison with our experiments because in all cases the densities of the two layers of the ambient differ by less than 5%. We show that the resulting formulae have a greatly simplified form to which perturbation theory may be straightforwardly applied. Thus, we are able to gain insight into the effect of relative depths and densities on the flow speeds through approximate analytic solutions.

By necessity, the theory does not allow for the generation of upstream or downstream waves. By comparing theory with experiments in circumstances in which

waves are generated, we are therefore able to assess the importance of wave generation on the evolution of the gravity current.

The paper is organized as follows. In § 2, we adapt the theory of Holyer & Huppert (1980) to the Boussinesq case and examine perturbation solutions in various limits. The experimental set-up and analysis methods are described in § 3 and qualitative results are presented in § 4. We compare observed flow speeds with theory in § 5 in which we further examine the properties of the observed waves. In § 6, we summarize our results and we develop empirical predictions for current speeds and wave characteristics based upon the experimental results.

2. Theory

Theoretical predictions of gravity current speeds based on mass, momentum and energy conservation were derived rigourously by Benjamin (1968). The theoretical speed†, U, of a gravity current of density ρ_ℓ propagating into an ambient fluid of density $\rho_0 < \rho_\ell$ and finite depth h_T is given implicitly by

$$\frac{U^2}{g'\Delta d} = \frac{(h_T - \Delta d)(2h_T - \Delta d)}{h_T(h_T + \Delta d)}, \tag{2.1}$$

in which Δd is the depth of the trailing tail sufficiently far behind the head and $g' = g(\rho_\ell - \rho_0)/\rho_{00}$ is the reduced gravity. Here, we have invoked the Boussinesq approximation so the density difference $\rho_\ell - \rho_0$ is normalized by a characteristic density ρ_{00}.

There are two limits of interest. For energy-conserving currents, $\Delta d = h_T/2$ and so (2.1) gives

$$U \to \sqrt{g'\Delta d/2}. \tag{2.2}$$

In the limit $h_T \gg \Delta d$, energy cannot be conserved in the context of Benjamin's theory. Nonetheless, the speed can be predicted by the equation

$$U \to \sqrt{2g'\Delta d}. \tag{2.3}$$

Here, Δd is the depth of the tail well behind the turbulent mixing region in the lee of the gravity current head.

In deriving the theory for the two-layer experiments, it is assumed that the thickness between the two layers is negligibly small. In the experiments, the interfacial thickness is typically found to be approximately 0.5 cm, an order of magnitude smaller than the height of the intrusion head.

The extension of Benjamin's theory to describe the dynamics of an interfacial gravity current was first developed by Holyer & Huppert (1980). Assuming a steady-state dissipationless flow that conserved mass and momentum, they derived a coupled set of cubic polynomial equations in two variables representing the relative depths of the fluid above and below the gravity current head. The numerical solution to these formulae revealed that the equations admitted three possible simultaneous solutions over a range of parameters.

† We adopt the convention throughout that $U_()$ represents theoretically predicted speeds and $C_()$ represents observed speeds, in which '()' is a subscript representative of the velocity in question. For example, U_{gc} and C_{gc} are the predicted and observed speeds, respectively, of intrusions along the interface of a two-layer fluid.

In order to gain insight into this behaviour, we apply the Boussinesq approximation to their equations (2.29) and (2.30), which we leave, for now, in dimensional form. Thus, we find the dynamics are set by the solution of the following two equations for mass and momentum conservation, respectively:

$$\alpha_0 h_0 r_0^2(1-r_0) = \alpha_1 h_1 r_1^2(1-r_1), \tag{2.4}$$

$$\alpha_0 h_0^2(1-r_0)^2(1-2r_0) + \alpha_1 h_1^2(1-r_1)^2(1-2r_1) = 0. \tag{2.5}$$

Here, $r_0 = h_0'/h_0$ and $r_1 = h_1'/h_1$, in which h_0' and h_1' represent the depth of the fluid above and below the gravity current, respectively, as illustrated in figure 1(*b*). The relative density differences are represented by $\alpha_0\sigma = (\rho_\ell - \rho_0)/\rho_{00}$ and $\alpha_1\sigma = (\rho_1 - \rho_\ell)/\rho_{00}$, in which for convenience, as will be made apparent below, we have introduced $\sigma = (\rho_1 - \rho_0)/\rho_{00}$, the relative density difference between the lower and upper ambient layers.

After solving for r_0 and r_1, the speed of the gravity current, $U_{\rm gc}$, is given by $U_{\rm gc} = r_1 U_1$ in which

$$U_1^2 = 2\alpha_1 g\sigma h_1(1-r_1). \tag{2.6}$$

Equivalently, $U_{\rm gc} = r_0 U_0$ in which

$$U_0^2 = 2\alpha_0 g\sigma h_0(1-r_0). \tag{2.7}$$

U_0 and U_1, respectively, represent the speeds of the return flows above and below the gravity current in a frame of reference moving with the gravity current head.

We rewrite (2.4) and (2.5) in non-dimensional form introducing parameters $H_0 = h_0/(h_T/2)$ and $H_1 = h_1/(h_T/2)$, characterizing the relative depth of the upper- and lower-layer ambient compared with half the total fluid depth h_T. In some circumstances, it is convenient to define

$$\Delta = (h_0 - h_1)/h_T \equiv (H_0 - H_1)/2, \tag{2.8}$$

which measures the relative difference in depths between the upper- and lower-layer ambient depths. In experiments in which the upper- and lower-layer fluids have equal depth, $H_0 = H_1 = 1$ and $\Delta = 0$.

To characterize the relative density differences between the gravity current (which originates from the lock) and the upper- and lower-layer ambient, we introduce the non-dimensional parameter

$$\epsilon = \frac{\rho_\ell - \bar\rho}{\rho_1 - \rho_0}, \tag{2.9}$$

in which $\bar\rho = (h_0\rho_0 + h_1\rho_1)/h_T$ is the mean density of the ambient fluid. Thus, experiments with $\epsilon = 0$ correspond to cases in which neither salt nor fresh water is added to the lock behind the gate before mixing. This parameter was originally introduced by de Rooij *et al.* (1999) in the special case with $h_0 = h_1$. The condition that $\rho_0 \leqslant \rho_\ell \leqslant \rho_1$ requires that $-(1-\Delta)/2 \leqslant \epsilon \leqslant (1+\Delta)/2$. In particular, if $h_0 = h_1$, then $\Delta = 0$ and ϵ ranges from $-1/2$ to $1/2$.

Using the definition for ϵ, we find

$$\alpha_0 = H_1/2 + \epsilon \equiv \frac{1-\Delta}{2} + \epsilon \tag{2.10}$$

and

$$\alpha_1 = H_0/2 - \epsilon \equiv \frac{1+\Delta}{2} - \epsilon. \tag{2.11}$$

Thus, the solutions to (2.4) and (2.5) are determined entirely by the parameters ϵ and Δ.

Solutions to the more general non-Boussinesq equations were found numerically by Holyer & Huppert (1980). They showed that three simultaneous solutions existed for a range of ϵ in a neighbourhood of $\epsilon = 0$, but that only one solution existed outside this range. In the former case, Holyer & Huppert (1980) proposed that the solution which would in fact be realized would be that for which the mass flux due to the gravity current was largest. The resulting prediction for values of r_0, r_1 and ultimately $U_{\rm gc}$ thus exhibited discontinuous jumps as a function of ϵ.

This seemingly unphysical prediction has, in part, inspired us to examine the pertubation theory solution to (2.4) and (2.5) for ϵ close to zero. The resulting explicit analytical solutions may then be compared with a range of experiments first with $\epsilon = 0$ (the lock fluid being established by simply mixing the upper- and lower-layer fluids), with $\epsilon > 0$ (salt being added to the lock fluid), and with $\epsilon < 0$ (the lock fluid being diluted with fresh water).

In the doubly symmetric case $\epsilon = 0$ and $H_0 = H_1 = 1$, (2.5) and (2.4) have a solution $r_0 = r_1 = 1/2$. This is consistent with the prediction by Benjamin (1968) that the depth of an energy-conserving gravity current is half that of the ambient fluid ahead of it.

We are interested in perturbations from this solution as ϵ differs by a small amount from zero. Thus, we define $\delta_0 = -(r_0 - 1/2)$ and $\delta_1 = r_1 - 1/2$. Substituting these expressions into (2.4) and (2.5), and using (2.10) and (2.11) gives

$$(H_1 + 2\epsilon)H_0(1 - 2\delta_0)^2(1 + 2\delta_0) = (H_0 - 2\epsilon)H_1(1 + 2\delta_1)^2(1 - 2\delta_1), \tag{2.12}$$

and

$$(H_1 + 2\epsilon)H_0^2\delta_0(1 + 2\delta_0)^2 = (H_0 - 2\epsilon)H_1^2\delta_1(1 - 2\delta_1)^2. \tag{2.13}$$

Next, we write δ_0 and δ_1 as perturbation expansions in ϵ: $\delta_i = \epsilon\delta_i^{(1)} + \epsilon^2\delta_i^{(2)} + \ldots$, for $i = 0$ and 1. Substituting these into (2.13) and (2.12), matching terms of successive powers of ϵ, and solving the resulting set of linear equations give the following:

$$r_0 \simeq \tfrac{1}{2} - \epsilon\frac{1}{1 + \Delta}\left(1 - 2\epsilon\frac{3 + \Delta}{\bar{H}^2} + 4\epsilon^2\frac{9 - 2\Delta + \Delta^2}{\bar{H}^4}\right), \tag{2.14}$$

$$r_1 \simeq \tfrac{1}{2} + \epsilon\frac{1}{1 - \Delta}\left(1 + 2\epsilon\frac{3 - \Delta}{\bar{H}^2} + 4\epsilon^2\frac{9 + 2\Delta + \Delta^2}{\bar{H}^4}\right). \tag{2.15}$$

Here, we have defined $\bar{H} \equiv (H_0H_1)^{1/2} \equiv (1 - \Delta^2)^{1/2}$ to be the geometric mean of H_0 and H_1. In the case of equal upper- and lower-layer depths, $\bar{H} = 1$.

Judging by the first three terms of the pertubation expansions above, and also by higher-order terms computed using the symbolic algebra package, 'Maple', the expansions converge provided $|\epsilon| \ll \bar{H}^2/6$. Indeed, in practice, we find the perturbation solutions converge to the numerically determined solutions of the full equations provided ϵ lies in the range where three simultaneous solutions exist.

The bounds on this range were first determined by Holyer & Huppert (1980) and are expressed here by $\epsilon_- < \epsilon < \epsilon_+$, where $\epsilon_- = -[2H_1 - 4/(1 + B_1)]$ and $\epsilon_+ = 2H_0 - 4/(1 + B_0)$. The values B_1^{-1} and B_0 are the bounds to α_0/α_1 where, explicitly,

$$B_i = \left[\frac{1}{3}\left(\frac{2}{H_i}\right)^{1/2} + 1\right]^3\left[\left(\frac{2}{H_i}\right)^{1/2} - 1\right],$$

for $i = 0$ and 1. Substituting $H_0 = 1 + \Delta$ and $H_1 = 1 - \Delta$ into the above conditions, the bounds on ϵ can be represented entirely as a function of one parameter, Δ. Indeed, it

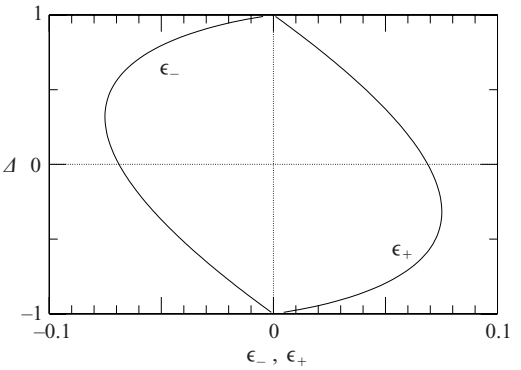

FIGURE 2. Predicted lower (ϵ_-) and upper (ϵ_+) bounds on perturbation theory expansion about $\epsilon = 0$.

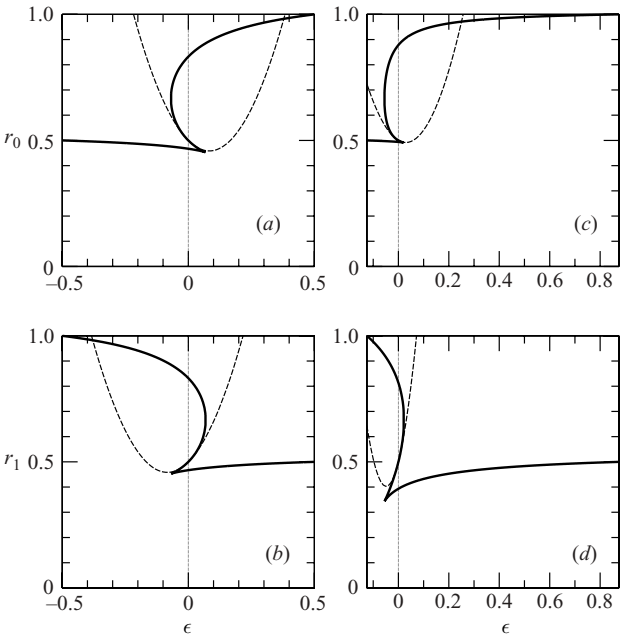

FIGURE 3. Relative depths of the return flow (a, c) above and (b, d) below the gravity current plotted in cases of a two-layer fluid (a, b) with equal depths ($\Delta = 0$) and (c, d) with a shallow lower-layer depth ($\Delta = 3/4$). The dashed lines show the second-order perturbation expansion about $\epsilon = 0$.

is a simple matter to show that $\epsilon_-(\Delta) = -\epsilon_+(-\Delta)$. These bounds on the convergence of the perturbation series for r_0 and r_1 about $\epsilon = 0$ are plotted in figure 2.

Figure 3 shows the predicted values of r_0 and r_1 versus ϵ for two values of Δ. Both the numerically computed exact solutions of (2.4) and (2.5) and the approximate perturbation solutions given by (2.14) and (2.15) are shown.

We have separately computed the solution to the general equations by Holyer & Huppert (1980) in the two circumstances shown. In both cases, the difference is negligible between the Boussinesq and non-Boussinesq solutions for a wide range of ϵ. In particular, for $H_0 = H_1 = 1$ and $\alpha_1\sigma = 0.01$, the magnitude of the difference

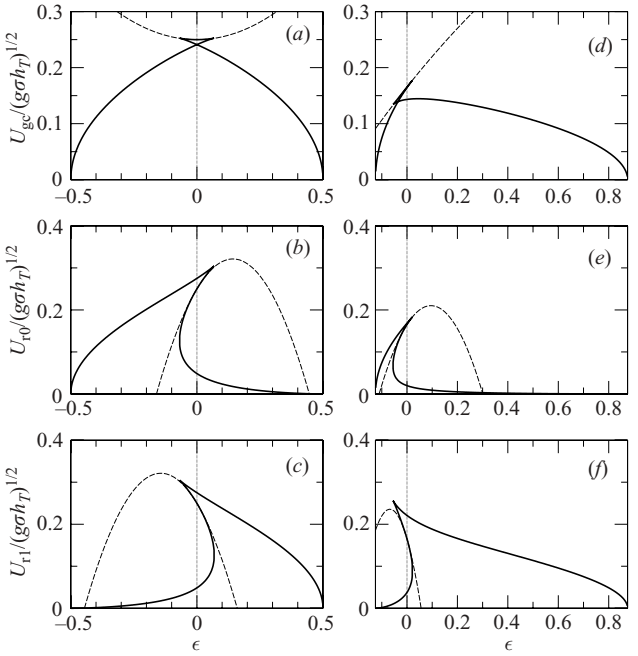

FIGURE 4. Normalized speeds of the (a, d) gravity current, (b, e) top return flow and (c, f) bottom return flow plotted in cases of a two-layer fluid $(a–c)$ with equal depths ($\Delta = 0$) and $(d–f)$ with a shallow lower-layer depth ($\Delta = 3/4$). The dashed lines show the second-order perturbation expansion about $\epsilon = 0$.

between the two solutions is less than 0.001 for ϵ as large as 0.4524 (corresponding to $\alpha_0\sigma = 2.0$).

Using (2.14) and (2.15) together with (2.6), we compute the speed of the gravity current, U_{gc}, to be given by

$$\frac{U_{gc}}{\sqrt{g\sigma h_T}} \simeq \frac{1}{4}(\bar{H})\left[1 + \frac{2\Delta}{\bar{H}^2}\epsilon + \frac{1-2\Delta^2}{\bar{H}^4}\epsilon^2\right]. \tag{2.16}$$

In particular, for $\epsilon = 0$, U_{gc} varies with Δ as $\bar{H} = (1-\Delta^2)^{1/2}$. For $\epsilon \gtrsim 0$ (in which case the density of the gravity current more closely matches that of the lower layer), the current speed is proportionally larger if the upper layer is deeper than the lower layer.

Figure 4 compares the exactly and approximately predicted speeds of the gravity current in cases with (a) $\Delta = 0$ and (d) $\Delta = 3/4$. In both circumstances, the second-order-accurate speed given by (2.16) is comparable with the exact solution over only a small range of ϵ compared with the entire range of values that ϵ can hold. Nonetheless, as we will show in § 5.1, the approximate solution is in fact a more accurate representation of the observed gravity current speeds.

We also compute the magnitude of the speed of the return flows, respectively, above and below the gravity current, $U_{r0} = U_0 - U_{gc}$ and $U_{r1} = U_1 - U_{gc}$, which are given in the frame of reference with a stationary ambient. Explicitly,

$$\frac{U_{r0}}{\sqrt{g\sigma h_T}} \simeq \tfrac{1}{4}(\bar{H})\left(1 + 2\frac{2-\Delta}{\bar{H}^2}\epsilon - 2\frac{7-4\Delta-2\Delta^2}{\bar{H}^4}\epsilon^2\right) \tag{2.17}$$

and

$$\frac{U_{\rm r1}}{\sqrt{g\sigma h_T}} \simeq \tfrac{1}{4}(\bar{H})\left(1 - 2\frac{2+\Delta}{\bar{H}^2}\epsilon - 2\frac{7+4\Delta-2\Delta^2}{\bar{H}^4}\epsilon^2\right). \tag{2.18}$$

The exact and approximate values of $U_{\rm r0}$ and $U_{\rm r1}$ for $\Delta = 0$ are plotted in figures 4(b) and 4(c), respectively, and for $\Delta = 3/4$ are plotted in figures 4(e) and (f), respectively.

Another limit of interest is that in which one layer is significantly deeper than the other. In particular, we examine the case in which $H_1 \ll H_0$. This case was also examined by Holyer & Huppert (1980) in the Boussinesq approximation. (Note, the corresponding figure they provide is correct, however, a typographical error exists in their equation (2.3.4)). In our notation, the change in depth r_1 of the lower-layer fluid is given by the solution of the quartic equation

$$\frac{1-\epsilon}{\epsilon} r_1^4 + 2r_1 - 1 = 0. \tag{2.19}$$

As shown in Appendix A, the approximations leading to this equation are justified provided $0 \ll \epsilon \lesssim 1$. Regular perturbation theory about $\epsilon = 1^-$ gives

$$r_1 \simeq \tfrac{1}{2} - \tfrac{1}{32}(1-\epsilon) - \tfrac{3}{128}(1-\epsilon)^2, \tag{2.20}$$

from which we estimate the gravity current speed to be

$$\frac{U_{\rm gc}}{\sqrt{g\sigma h_T}} \simeq \tfrac{1}{4}(\bar{H})(1-\epsilon)^{1/2}\left[1 - \tfrac{1}{32}(1-\epsilon)\right]. \tag{2.21}$$

Converting (2.21) into a form that does not depend explicitly on the upper-layer depth (which we now take to be infinitely large), we find

$$\frac{U_{\rm gc}}{\sqrt{g\sigma h_1}} \simeq \tfrac{1}{2}(\alpha_1)^{1/2}\left[1 - \tfrac{1}{32}(\alpha_1)\right]. \tag{2.22}$$

in which $\alpha_1 = (\rho_1 - \rho_\ell)/(\rho_1 - \rho_0)$ must be small (i.e. $\rho_\ell \lesssim \rho_1$).

In particular, in the limit $\rho_0 \to 0$, using $r_1 = 1/2$ we find $U_{\rm gc} \simeq (g\alpha_1 h_1)^{1/2}/2$. This is the same result found for an energy-conserving gravity current propagating into uniform fluid, as given by (2.2) with $\Delta d = h_1/2$.

3. Experimental set-up and analysis

Experiments are performed in a glass tank of length $L = 197.1$ cm, width 17.6 cm and height 48.5 cm, as shown in figure 1. A two-layer fluid is established by first filling the tank to a depth h_1 with salt water of density ρ_1. Fresh water, of density ρ_0, is then added such that it forms an additional layer of depth h_0. The fresh water is poured through a sponge float to reduce interfacial mixing. A vertically traversing 50 cm long fast conductivity and temperature probe (Precision Measurement Engineering) is used to measure the resulting density profile and to confirm that the interface between the two fluids is negligibly thin (typically with half-thickness less than 0.5 cm) compared with the depth of the gravity current head.

Experiments are performed so that the total depth $h_T = h_0 + h_1$ is either 20 cm or 40 cm. Relative values of h_0 and h_1 are examined so that Δ, defined by (2.8), ranges approximately between $-3/4$ and $7/8$. Values of ρ_1 are chosen so that the relative density difference σ ranges approximately between 0.005 and 0.050. The resulting Reynolds number of the flow, based on the intrusion speed and ambient half-depth, ranged from 1000 to 20 000 with typical values of $Re \sim 5000$, corresponding to intrusions moving at speeds of 5 cm s^{-1} in fluid with half-depth $h_T/2 = 10$ cm.

After the two-layer fluid is established- a water-tight gate is inserted into one of five guides composed of 1 mm thin glass strips on either side of the tank. These permit the gate to be rapidly vertically extracted. The resulting lock established behind the gate has length $\ell = 8.5$, 18.6, 28.6, 38.5 or 48.5 cm. Most experiments are performed with $\ell = 18.6$ cm as the characteristics of the intrusion and waves are found to be similar for the other four lock-lengths.

In experiments with $\epsilon = 0$, the gate is inserted and the two layers of fluid in the lock are well mixed so that the lock is filled with fluid of uniform density $\bar{\rho} = (h_0\rho_0 + h_1\rho_1)/h_T$. This establishes the final lock-fluid density, ρ_ℓ (e.g. see (2.9)).

In experiments with $\epsilon > 0$, salt is added to the lock prior to mixing so that the fluid density is increased, but not so much that the final lock-fluid density, ρ_ℓ, is greater than ρ_1.

Experiments with $\epsilon < 0$ follow a slightly different procedure. After the gate is inserted, a pre-established volume of salt water is siphoned from the lower layer of fluid in the lock and an equal volume of fresh water is added to the top layer. Only after this transfusion is the lock fluid well mixed to give a fluid of density ρ_ℓ. Values of ρ_ℓ are chosen so that ϵ ranges approximately between -0.2 and 0.65.

A digital camera is positioned 3.5 m from the front of the tank and is set up to be level with the depth of the interface between the upper- and lower-layer fluids. The whole length of the tank is in the camera's field of view.

In order for the camera to visualize the collapse and structure of the gravity current after the gate is released, a small amount of blue food colouring is first mixed into the lock fluid. Typically 10 ml of dye is added, an amount that negligibly changes the density of the lock fluid. Once the solution in the lock is calm (approximately 30 s), the gate is quickly removed and the resulting dynamics are recorded on tape. In some experiments, the interface between the two layers of ambient fluid is also marked by adding a small quantity of red food colouring to the sponge float during initial stages of layering on the fresh water.

Using 'DigImage' software, the position of the gravity current as a function of time is determined from digitized horizontal time-series images of the experiments (Dalziel 1992). These images are constructed by successively stacking in time horizontal slices through the movie images with the slices taken at the level of the two-layer fluid interface. The time between slices can be as small as $\Delta t = 1/30$ s. The front of the gravity current can be identified in the time series by the diagonal contour separating the darkly dyed intruding lock fluid and the relatively light ambient. The velocity of the gravity current head, $C_{\rm gc}$, is determined by finding the slope of the best-fit line to the position versus time data over a fixed spatial range.

Likewise, time series constructed by taking horizontal slices at distances $(3/4)h_0$ above and $(3/4)h_1$ below the interface are used to determine $C_{\rm r0}$ and $C_{\rm r1}$, the velocity of the top and bottom return flows, respectively (see figure 1*b*).

After the return flows encounter the rear wall of the tank, top and bottom forward-moving rear bores may be established (see figure 1*c*). The bore speeds, respectively, $C_{\rm b0}$ and $C_{\rm b1}$, are determined when possible from horizontal time series taken $(1/4)h_0$ above and $(1/4)h_1$ below the interface.

The horizontal time series and, in particular, those at the level of the interface may also be used to measure the speed, $C_{\rm wv}$, and horizontal extent, λ, of the interfacial wave that propagates ahead of the intrusion in some experiments, particularly those with $\epsilon \neq 0$ (see figure 1*c*). We also construct vertical time series from a vertical slice through the movie images at a range of distances from the lock. These are used to measure the amplitude, $A_{\rm wv}$, of the leading wave. Typically, the measurement is

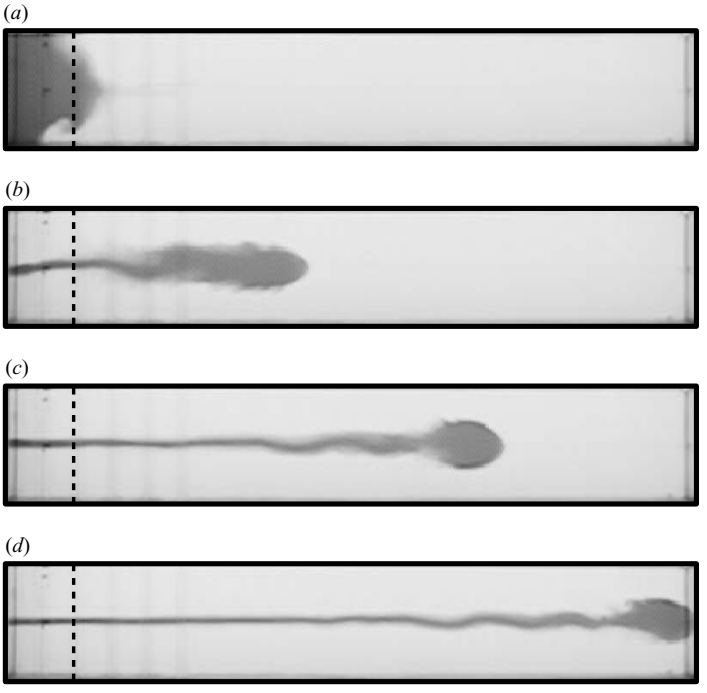

FIGURE 5. Snapshots of gravity current in experiment with $h_0 = h_1 = 10\,\text{cm}$, and $\alpha_1\sigma = \alpha_0\sigma = 0.01$ ($\Delta = 0$, $\epsilon = 0$). The gate, whose initial position is illustrated with the vertical dashed line superimposed on each image, is extracted at time $t = 0$. Snapshots are taken at (*a*) $t = 2\,\text{s}$; (*b*) 14 s; (*c*) 26 s; (*d*) 38 s.

made from a vertical time series taken from a vertical slice halfway along the tank (approximately four lock-lengths from the gate in most experiments).

4. Qualitative results

The experiments exhibit a remarkably rich variety of dynamics depending on the values of Δ and ϵ. For fixed Δ and ϵ, however, the qualitative properties and quantitative measurements do not depend explicitly on h_T, σ and ℓ.

The range of behaviours is illustrated in this section with the presentation of successive snapshots and time series taken from four representative experiments. In each, $h_T = 20\,\text{cm}$, $\sigma = 0.02$ and $\ell = 18.6\,\text{cm}$.

Figure 5 shows snapshots taken every 12 s of the full length of the tank for an experiment in which $\Delta = \epsilon = 0$. This is the well-studied doubly symmetric case (Britter & Simpson 1981; de Rooij *et al.* 1999; Mehta *et al.* 2002) in which the upper- and lower-layer fluid depths are equal and the density of the lock fluid is the average of the upper and lower layers.

Two seconds after the lock is released (figure 5*a*), the forward collapse of the intrusion and the coincident return flows above and below the intrusion are evident. At time $t = 14\,\text{s}$, the top rear bore, which advances toward the gravity current head, is evident close to one lock length from the original position of the gate. After another 12 s, the rear bore catches up with the gravity current head which then maintains an oblong shape until it encounters the end of the tank after 38 s.

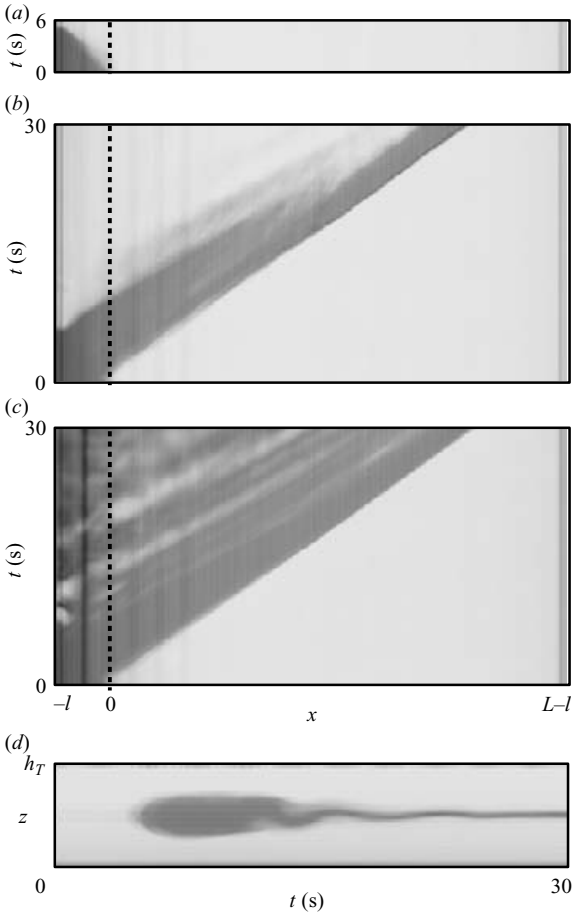

FIGURE 6. Horizontal time series taken at depth (with respect to the bottom of the tank) (*a*) $(7/8)h_T$, (*b*) $(5/8)h_T$ and (*c*) $(1/2)h_T$, and (*d*) vertical time series taken one lock length to the right of the gate. The images are extracted from the same experiment as that shown in figure 5.

Although the interface is not dyed in this particular experiment, in general, we observe no significant deflection of the interface in these doubly symmetric experiments. On the other hand, the thin tail behind the gravity current head does exhibit weak undulations representative of interfacial internal waves.

These dynamics are best illustrated with the time series images shown in figure 6. The horizontal time series taken at the level of the interface (figure 6*c*) shows the steady advance of gravity current head into the ambient. The diagonal bands behind the front result from the trailing undulations of interfacial internal waves. Note that the speed of these waves is moderately larger than that of the gravity current, a feature observed by Mehta *et al.* (2002) in their study of intrusions in two- and three-layer fluids. The frequency, amplitude and decay of the waves with time after the gravity current passes are also apparent in the vertical time series in figure 6(*d*).

The horizontal time series taken $(3/4)h_0$ above the level of the interface ($(7/8)h_T$ above the bottom of the tank) is shown in figure 6(*a*). It clearly illustrates the return flow of the ambient fluid into the lock after the gate is released. After the return flow

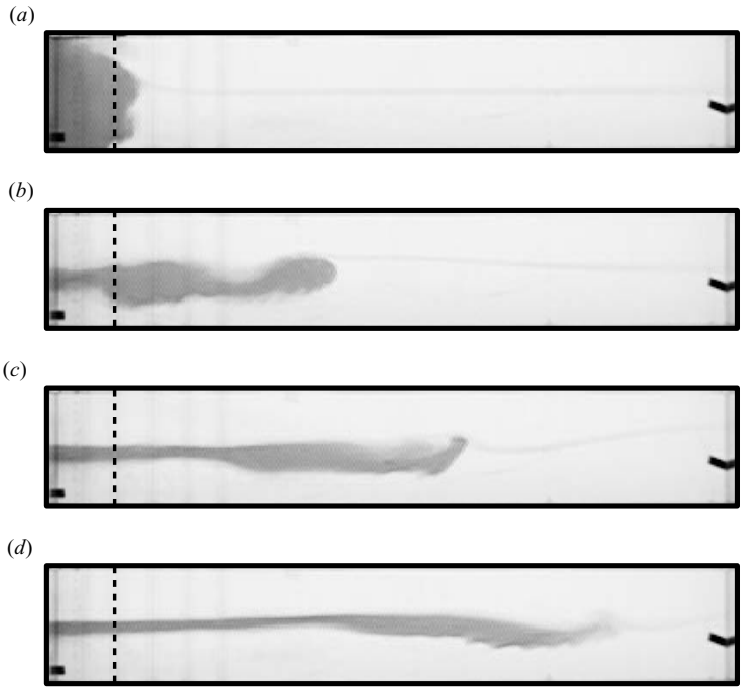

FIGURE 7. As in figure 5 but for experiment with $h_0 = h_1 = 10\,\text{cm}$, and $\alpha_0\sigma = 3\alpha_1\sigma = 0.015$ ($\Delta = 0$, $\epsilon = 0.25$).

reflects from the rear wall of the tank, the depth of the ambient above the intrusion increases and a rear bore develops that moves toward the gravity current head as illustrated by the horizontal time series taken $(1/4)h_0$ above the interface, as shown in figure 6(*b*).

A curious feature of these experiments is that the gravity current speed does not decrease after the rear bore catches up with the gravity current head (at time $t \simeq 18\,\text{s}$ in the experiment shown in figures 5 and 6). This behaviour is different from that of gravity currents that move along the bottom of a uniform ambient, in which case the gravity current speed is well known to decrease, typically after it has propagated 6 to 10 lock lengths (see Rottman & Simpson 1983; Sutherland 2002; and, in particular, figure 4 of Mehta *et al.* 2002). Why an intrusive gravity current does not decelerate remains an open question whose investigation is beyond the scope the present study.

Figure 7 shows snapshots taken from an experiment in which the upper- and lower-layer fluids have equal depth ($\Delta = 0$), but salt is added to the lock-fluid so that $\epsilon \simeq 1/4$. The change in behaviour of the gravity current is striking. Most notably, the gravity current does not propagate to the end of the tank, but stops after propagating a distance of approximately 6 lock lengths. Ahead of the gravity current, an interfacial internal wave is generated. Finally, in observations made more clear from moving images of the experiment, the top rear bore catches up with the gravity current head at time $t \simeq 26\,\text{s}$ and thereafter passes it, resulting in the flattening of the head between times $t \simeq 26$ and $t \simeq 38\,\text{s}$.

These dynamics are illustrated more clearly in figure 8 which shows the speed of advance of the interfacial wave as the most shallow diagonal contour that marks the rise above $z = h_T/2$ of the initially dyed interface. The initial speed of advance of

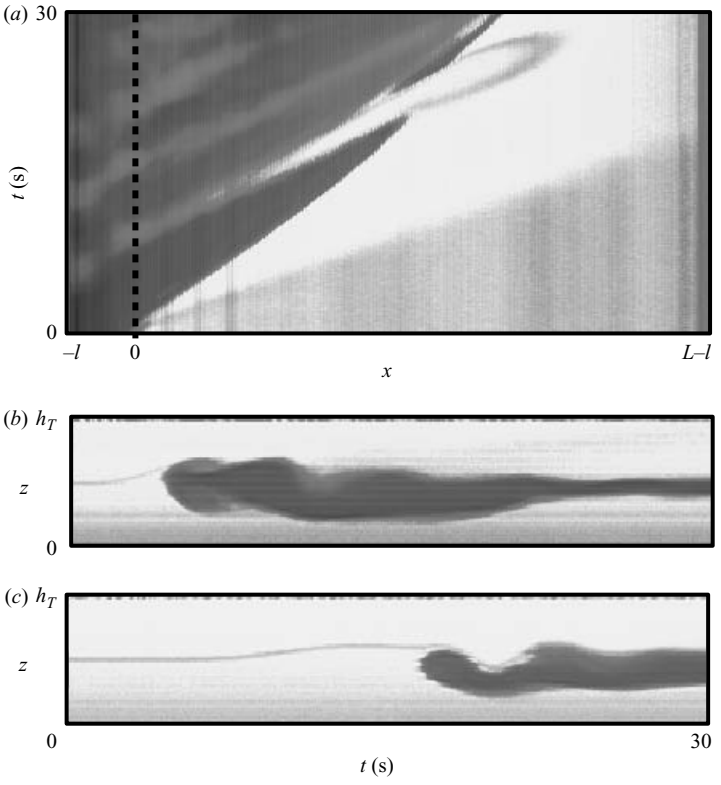

FIGURE 8. Horizontal time series taken at depth (*a*) $(1/2)h_T$ and vertical time series taken (*b*) 1 and (*c*) 4 lock lengths from the gate. The images are extracted from the same experiment as that shown in figure 7.

the gravity current head is indicated by the slope of the contour between the dark-dyed fluid and the lighter ambient. Finally, the speed of the rear bore is apparent in this figure from the slope of the contour that intersects the contour that tracks the front of the gravity current head midway along the tank. It is the fact that the contours intersect rather than asymptotically become parallel that indicates the strong interaction between the top rear bore and the gravity current head. Over the 30 s shown, the bore obviously retards the progress of the intrusion. Longer time series confirm that the intrusion stops advancing altogether after approximately 40 s.

Comparing the vertical time series in figures 6(*d*) and 8(*b*), the latter shows that the tail behind the gravity current head remains thick for a long time after the front of the head has passed. It also shows that the amplitude of the leading interfacial wave is comparable to the height of the gravity current head above the interface. Figure 8(*c*) shows that further from the lock (approximately half-way along the tank), the tail remains thick behind the head even after it is deformed by the top rear bore and the interfacial wave crests near the gravity current head at this position.

The dynamics are different again if the relative depths of the upper- and lower-layer fluids are not equal. For example, figure 9 shows snapshots taken from an experiment with $\Delta \simeq 3/4$ and $\epsilon = 0$. As in the experiment shown in figure 5, no salt is added to the lock and similarly we observe negligibly small amplitude leading interfacial internal waves. There are several differences, however. The gravity current head propagates less quickly along the tank and it is not symmetrically shaped: its underside is almost

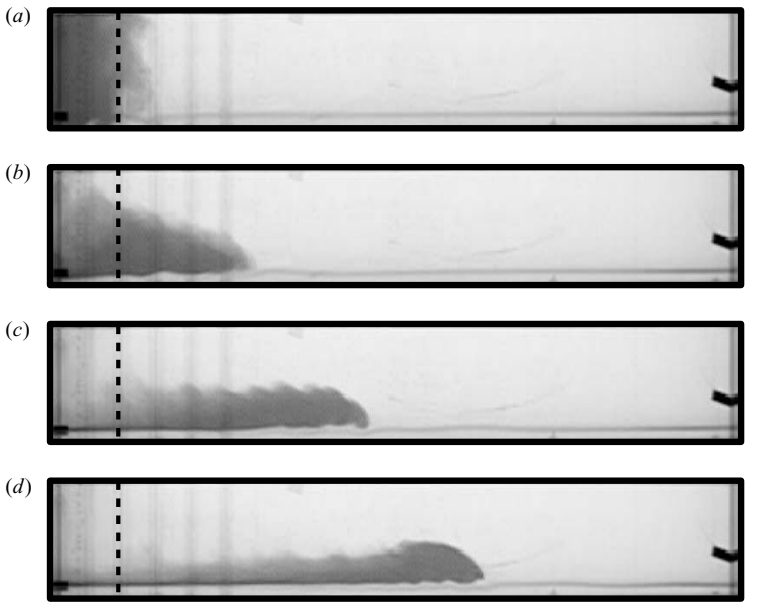

FIGURE 9. As in figure 5 but for experiment with $h_0 = 7h_1 = 17.5\,\mathrm{cm}$ and $\alpha_1\sigma = 7\alpha_0\sigma = 0.0175$ ($\Delta = 0.75$, $\epsilon = 0$).

flat whereas there is significant mixing on the upper flank of the head and trailing behind it for several lock-lengths.

Because the density difference between lock and ambient upper-layer fluid is small, the top return flow takes some time to become established. Indeed, mixing between the lock and ambient fluid is dominated initially by the vorticity introduced by the extraction of the gate. At later times, the front sharpens and adopts a form similar in appearance to that of a classic gravity current which propagates over a rigid bottom with a uniform ambient above. There is a subtle difference, however. The underside of the gravity current shown in figure 9(*d*) exhibits small undulations with typical wavelength smaller than the extent of the gravity current head. These are the result of a weak stratified shear instability in which waves grow at the interface between two fluids of different density and moving at different speeds.

The dynamics of the gravity current and interfacial disturbances are shown in figure 10. The horizontal time series, taken along the level of the interface shows weak leading interfacial waves but, as is apparent from the vertical time series, the amplitude of the waves is small. The undulations on the underside of the current result in the diagonal stripes in the horizontal time series image. The image shows that the phase speed of the undulations is close to the gravity current speed. A more in-depth analysis of these undulations is presented in Flynn & Sutherland (2004).

Finally, we present the case where $\Delta \simeq 3/4$ and $\epsilon \simeq 5/8$. The parameters for this experiment are similar to those for the experiment shown in figure 7 in that the corresponding densities of the upper-, lower- and lock-fluid are the same.

Snapshots are shown in figure 11. During the initial collapse of the lock fluid into the ambient, the gravity current propagates with its underside moving along the bottom of the tank. The current drives ahead of it an interfacial wave similar to that seen in experiments by Rottman & Simpson (1989), who studied gravity currents moving along the bottom of a two-layer fluid. In the present case, however,

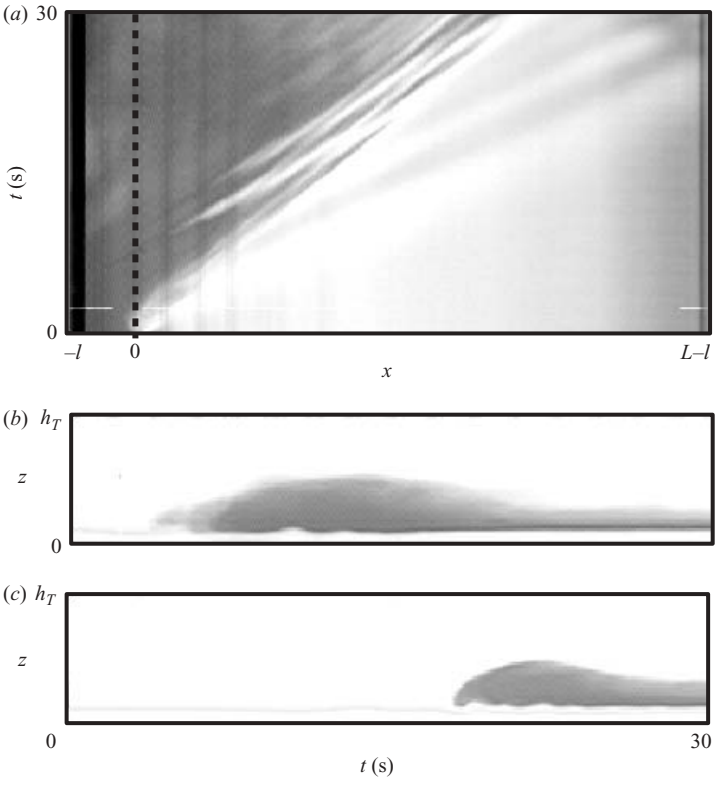

FIGURE 10. As in figure 8 but for the experiment with parameters given in the caption to figure 9.

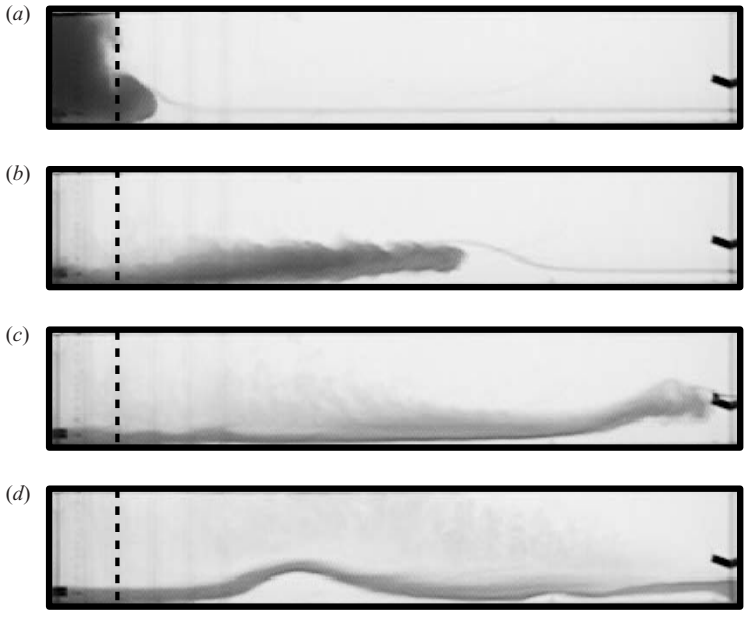

FIGURE 11. As in figure 5 but for experiment with $h_0 = 7h_1 = 17.5\,\mathrm{cm}$ and $\alpha_0\sigma = 3\alpha_1\sigma = 0.015$ ($\Delta = 0.75$, $\epsilon = 0.625$). The solitary wave in the bottom image propagates from right to left after having reflected from the right-hand wall of the tank.

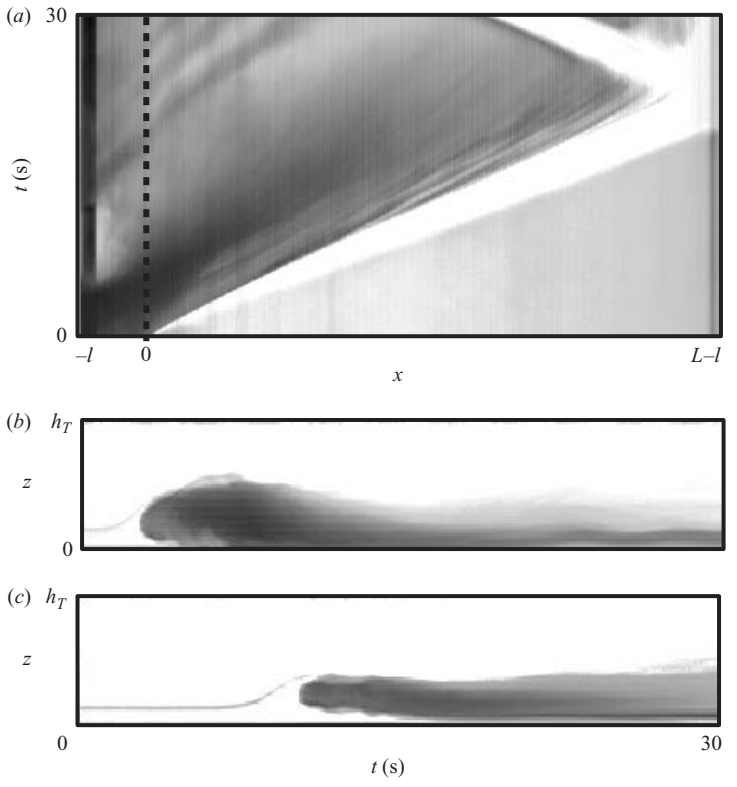

FIGURE 12. As in figure 8 but for the experiment with parameters given in the caption to figure 11.

the gravity current has a smaller density than the ambient lower-layer fluid and it therefore ultimately rises above the tank bottom, as shown in figure 11(*b*).

No rear bore is apparent in this experiment. However, the gravity current head does flatten out as it propagates along the tank. The current propagates quickly with speed comparable to that of the leading interfacial wave. The wave itself is clearly a nonlinear solitary wave: the disturbance is hump-shaped and during its passage it displaces fluid parcels in the lower layer by a distance comparable to the horizontal extent of the wave (not shown).

The time series images in figure 12 should be compared with the corresponding images in figure 8. Here, the gravity current head is clearly unaffected by disturbances behind the front catching up to it. The vertical time series shows that the amplitude of the interfacial wave is comparable to that of the gravity current head but the time scale for the interface to move from equilibrium to crest is significantly shorter.

5. Quantitative results

5.1. *Gravity current speed*

The speed of the gravity current is determined from the slope of the contour that tracks the front of the gravity current in horizontal time series taken along the interface of the two-layer ambient such as that shown in figure 6(*c*). The best-fit line through the contour is determined between 1 and 3 lock-lengths downstream of the gate and the inverse slope of this line gives the speed.

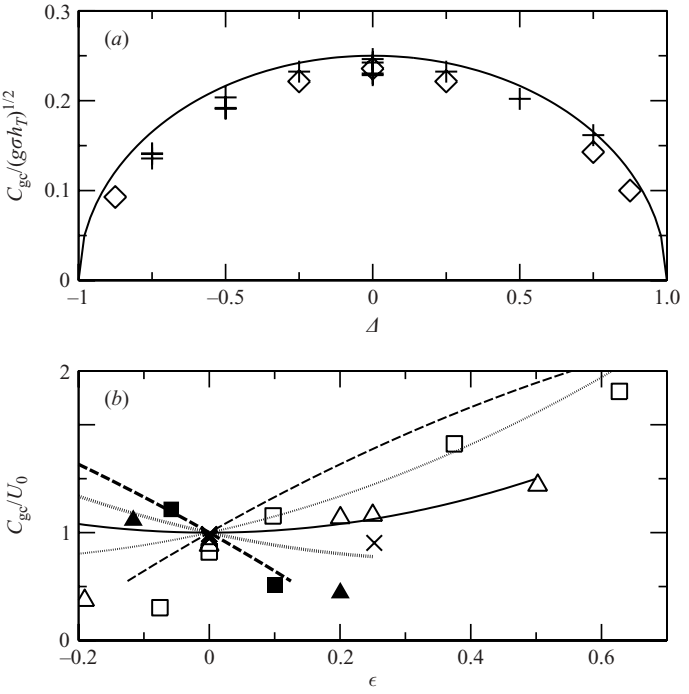

FIGURE 13. Normalized gravity current speeds in experiments with (*a*) no salt added and (*b*) with salt added to the lock after mixing. In (*a*), data are shown for experiments with total depths h_T equal to 20 cm (plus sign) and 40 cm (diamond). The solid line represents the theoretically predicted normalized speed, $\bar{H}/4$. In (*b*), symbols correspond to experiments with $h_T = 20$ cm and Δ equal to 3/4 (open square), 1/2 (open triangle), 0 (cross), $-1/2$ (closed triangle) and $-3/4$ (closed square). The line styles and weights correspond to the second-order accurate speeds predicted by theory in the cases with Δ equal to 3/4 (long-dash light), 1/2 (dotted light), 0 (solid light), $-1/2$ (dotted heavy) and $-3/4$ (long-dash heavy). The velocity data and theoretical curves are normalized by $U_0 = [(g\sigma h_T)^{1/2}]\bar{H}/4$.

The results of experiments with lock-length $\ell \simeq 18.6$ cm are shown in figure 13. Results, not shown, from experiments with half and with twice this lock length are similar for given Δ and ϵ.

Figure 13(*a*) shows the results of experiments with $\epsilon = 0$, in which case the lock density is established simply by mixing the ambient fluid behind the gate. Experiments with two different total depths are indicated by different symbols. The data also represent experiments with a range of σ. When the speeds are normalized by $(g\sigma h_T)^{1/2}$ and the points are plotted against Δ, the data collapse onto a curve whose shape is represented well by the theory given by (2.16), although the theory generally overpredicts the observed current speed by 5–10%.

The discrepancy can be explained in part by the thickness of the ambient two-layer fluid interface, which is assumed to be zero in theory but in experiments is typically $\delta \lesssim 1.0$ cm. The empirical formula by Faust & Plate (1984) predicts that the speed of doubly symmetric gravity currents should decrease with interface thickness as $0.58\delta/h_T$, which is approximately 3% in experiments with $h_T = 20$ cm. As demonstrated by Lowe *et al.* (2002) in their detailed analysis of symmetric intrusive gravity currents, despite mixing behind the head, the velocity was found to be close to that predicted for energy-conserving currents, presumably because the energy loss

is negligibly small compared to the energy of the system as a whole. Thus, we do not believe that dissipation can account for the small discrepancy we observe in our experiments with ϵ. Nor do we anticipate dissipation should play a significant role in any of our experiments.

In cases with non-zero ϵ, the agreement of theory with experiment is not as strong, though the trends are captured qualitatively. Figure 13(*b*) shows the results of experiments with a range of Δ and ϵ. The velocity data is collapsed by normalizing the observed speeds $C_{\rm gc}$ by $U_0 = (g\sigma h_T)^{1/2}\bar{H}/4 \equiv (g\sigma h_0 h_1/h_T)^{1/2}/2$. For clarity, only those experiments with $\sigma \simeq 0.02$ and $h_T = 20\,\text{cm}$ are shown (as the plotted symbols), though data computed from experiments with other σ and h_T collapse within errors to the corresponding values plotted here.

The second-order accurate theoretical predictions, given by (2.16) and plotted by lines in the figure, generally overpredict the observed speed by as much as 50%, the agreement being worse for larger $|\Delta|$. Nonetheless, the approximate solutions qualitatively capture the observed trends: the normalized speeds increase with increasing ϵ if Δ is positive and decrease with increasing ϵ if Δ is negative. The rate of increase is larger as Δ becomes larger.

This result is at first surprising because it implies that the asymptotic approximation predicts the actual behaviour better than the exact solution. Consider, for example, the approximate and exact speeds predicted in the case $\Delta = 3/4$, which are plotted in figure 4(*d*) by the dashed and solid lines, respectively. The approximate prediction is also plotted in figure 13 by the long-dashed light line. The approximate theory diverges significantly from the exact theory for $\epsilon \lesssim -0.02$ and $\epsilon \gtrsim 0.05$ (as given by the bounds $\epsilon_\pm$ plotted in figure 2) and increases monotonically for all ϵ. In contrast, the exact theory discontinuously jumps from an increasing solution near $\epsilon = 0$ to a monotonically decreasing solution for $\epsilon \gtrsim 0.05$.

Even in the absence of observational evidence, we might anticipate the complicated structure of the exact solution would not occur in reality. The discontinuous change in velocity for $\epsilon \simeq \epsilon_\pm$ is an artefact of the restrictive assumptions employed to formulate the exact theory.

One of these restrictions is that internal waves cannot develop ahead of the gravity current on the interface of the two-layer fluid. This assumption turns out to be valid in the case $\epsilon = 0$ because experiments show there is indeed negligible motion of the interface ahead of the gravity current. In this case, the gravity current speed is predicted well by theory. The experiments show, however, that large-amplitude internal waves are generated in experiments with non-zero ϵ. Apparently, the process of generating these waves dominates the dynamics governing the motion of the gravity current in a manner that is not captured by the exact theory of Holyer & Huppert (1980).

To illustrate the consequence of allowing non-steady upstream disturbances, consider the case $\epsilon \simeq 5/8$ and $\Delta \simeq 3/4$, for which snapshots of an experiment are shown in figure 11. Here, the gravity current density is greater than that of the average of the upper and lower layers and so it penetrates more deeply into the shallow lower layer. If, in theory, the interface ahead of the current does not support waves, the lower-layer ambient must overcome the potential energy of the current in order to pass underneath it. This must be done at the expense of the kinetic energy of the system, hence the gravity current must propagate relatively slowly. On the other hand, if the leading interface can support waves, then the lower-layer ambient fluid can be pushed ahead of the current as well as passing underneath it. Thus, the gravity current can propagate more quickly, as indeed we observe.

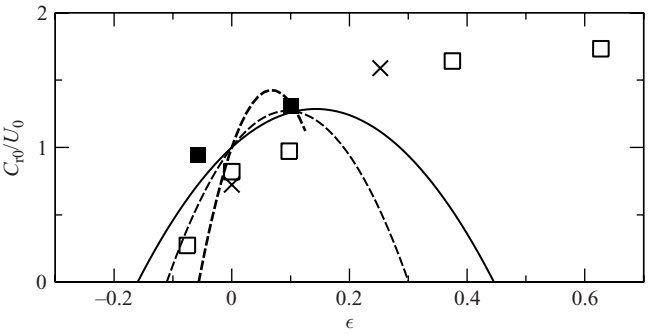

FIGURE 14. Normalized speeds of return flow in the upper layer determined from experiments with $h_T = 20\,\text{cm}$ and $\sigma \simeq 0.02$. The symbols and lines are plotted as in figure 13 but, for clarity, only those results for $\Delta = 0$ and $\pm 3/4$ are plotted.

5.2. *Return flow speeds*

Experimental determination of the speeds C_{r0} and C_{r1} of the top and bottom return flows, respectively, in the lock is difficult because the distance over which the speeds can be measured is limited. It is particularly difficult to measure in a shallow layer because the return flow is partially obscured by mixing between the fluid entering and exiting the lock.

For these reasons, we restrict our analysis here to measurements of the top-return flows in experiments where their speeds are unambiguously determined. Figure 14 plots as a function of ϵ values of C_{r0} normalized by U_0. As in figure 13, we find good agreement between experiments and the approximate theory given by (2.17) provided $|\epsilon| \lesssim 0.1$. However, both the approximate and exact theory significantly underpredict the observed speed in experiments with large ϵ and $\Delta = 0$ and 3/4 (e.g. see figure 4*b*, *e*).

We conclude that when ϵ is significantly different from zero, the upstream dynamics are important not only in controlling the gravity current speed but also the return flow speeds.

5.3. *Rear-bore/lee-wave speeds*

In experiments of full-depth lock-release bottom-propagating gravity currents in a uniform ambient, Rottman & Simpson (1983) showed that after the return flow encounters the end-wall of the tank, a forward-moving rear-bore develops. This is characterized by an internal hydraulic jump in which the ambient flow deepens and the tail of the gravity current becomes shallower over a short distance. The advance of this effective front is 20–30% faster than the speed of the gravity current and ultimately catches up with the gravity current head after it has travelled 6 to 10 lock lengths.

These dynamics are evident in intrusion experiments as well except that two rear bores can potentially develop: a top rear-bore resulting from the reflection of the top return flow off the endwall of the lock, and a bottom rear bore developing from the bottom return flow. These bores are schematically represented in figure 1(*c*) with top and bottom speeds indicated by C_{b0} and C_{b1}, respectively. The evolution of the observed rear bores are more complicated, however. Because both advancing fronts are connected through the thick density interface of the gravity current tail, they can collectively undulate vertically up and down through the excitation of an internal wave at this interface.

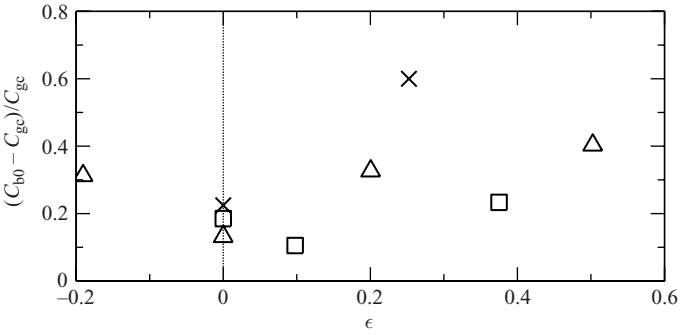

FIGURE 15. Speed of the rear-front (either rear-bore or lee wave) along upper interface relative to measured intrusion speed determined from experiments with $h_T = 20\,\text{cm}$ and $\sigma \simeq 0.02$. The symbols are plotted as in figure 13.

The excitation of internal waves through this process was investigated by Mehta *et al.* (2002) who examined doubly symmetric intrusions in two-layer fluids with $\epsilon = \Delta = 0$ and in three-layer fluids with corresponding symmetry. The three-layer fluid was formed as a consequence of repeatedly releasing doubly symmetric intrusions along an interface that successively thickens as lock fluid transported by the intrusions is deposited along the fluid's mid-depth. The experiments showed that sinusoidal internal waves developed in the lee of the gravity current head and the amplitude and number of waves increased as the thickness of the middle layer deepened.

In our asymmetric experiments we likewise find that interfacial waves rather than advancing bores are predominant in the lee of the gravity current head. The structure of the interfacial waves is more complicated, however. Whereas trailing sinusoidal waves are observed in three-layer experiments – a result of resonant coupling between waves on the interfaces above and below the middle layer – we find that the trailing waves do not have such a symmetric structure if ϵ is non-zero. Similar to the three-layer experiments, we find the trailing waves not only catch up to the gravity current head like a rear-bore catches up to a bottom-propagating gravity current, but the waves can move through and pass the interfacial gravity current head. When this occurs, the head is deformed and halts its steady advance. Such behaviour is evident, for example, in time series images such as that in figure 8(*a*).

Figure 15 shows the observed speed of the advancing rear-front (either a bore or a lee-wave) along the upper interface behind the gravity current head. Typically, measurements are taken from horizontal time-series over distances between one and three lock-lengths from the lock-end of the tank. The differences between the rear-front speed C_{b0} and the gravity current speed C_{gc} are plotted as a function of ϵ. In all cases, the rear-front speed is faster than the gravity current speed.

If $\epsilon = 0$, we find the rear-front catches up to the gravity current head, but does not pass it. The head instead assumes an approximately steady-state shape. If $\Delta = 0$, this shape is in the form of a rounded bulge symmetrically above and below the interface with a trailing tail of approximately constant depth. If Δ is non-zero, the rounded bulge is more pronounced in the deeper layer and undulations appear along the interface between the gravity current and the more shallow layer. Generally, we find the rear-front speed is 10–20% faster than the gravity current speed.

If $|\epsilon|$ is sufficiently large, the rear-front speed is substantially larger than the gravity current speed. It is almost 60% faster in experiments with $\Delta = 0$ and $\epsilon \simeq 1/4$. The relative difference in speeds is smaller as Δ increases.

There is a corresponding qualitative change in the dynamics of the gravity current head. In experiments with $\Delta = 0$ and $\epsilon > 0$, the rear-front passes the gravity current head which deforms it and halts its advance. In experiments with $\Delta > 0$ and $\epsilon > 0$, the gravity current head has a flattened shape shortly after it is formed but advances at an approximately constant speed while a solitary wave develops in the shallow layer ahead of the intrusion.

The bottom-propagating gravity current experiments of Rottman & Simpson (1983) showed that the gravity current head decelerated to a new but constant speed after the rear-bore catches up with it. Our experiments demonstrate the dynamics are more complicated for an interfacial gravity current. If no interfacial waves are generated ahead of the current ($\epsilon = 0$) the head propagates at constant speed well beyond 6 to 10 lock lengths. Likewise, the head propagates at constant speed if $|\Delta|$ is sufficiently large that solitary waves are efficiently generated in the shallow layer ahead of the current. Presumably this is because the relatively small-amplitude rear-fronts are damped when they interact with the trailing edge of the solitary wave. However, if $\Delta \simeq 0$, classical Korteweg–de Vries solitary waves cannot exist in the ambient fluid ahead of the gravity current. If ϵ is sufficiently large that the gravity current head propagates predominantly below the interface of the equal-depth two-layer fluid, the rear-front is not inhibited from passing over the current head. The resulting transport of momentum from the lee to the fore of the head induces a deceleration to the interfacial flow which halts it.

Though we have presented a qualitative argument for the observed dynamics, it remains to develop a quantitative theory which predicts the gravity current speed and the transition in its behaviour. Developing such an analytic theory is beyond the scope of the present work. However, the analysis of the leading interfacial waves below and the empirical analysis in § 6 serve to provide data that would be useful in the development of such a theory.

5.4. *Interfacial wave*

Figure 16 shows measured values of the leading interfacial wave speed $C_{\rm wv}$ relative to the observed gravity current speed $C_{\rm gc}$ and the predicted two-layer small-amplitude shallow-water wave speed $U_{\rm sw}$. Explicitly, $U_{\rm sw}$ is given by (e.g. see Gill 1982)

$$U_{\rm sw} = (g\sigma h_{\rm sw})^{1/2} \equiv 2U_0, \tag{5.1}$$

in which $h_{\rm sw} = h_0 h_1 / h_T \equiv \bar{H}^2 h_T / 4$.

Figure 16(a) plots the relative difference $C_{\rm gc} - U_{\rm sw}$ as a function of ϵ. Only cases with $\epsilon > 0$ and $\Delta > 0$ are plotted. For small Δ, the gravity current speed is smaller than the shallow-water speed for all ϵ, though the magnitude of the difference decreases as ϵ increases. When Δ is sufficiently large, however, the gravity current speed can exceed the shallow-water speed provided ϵ is large enough. For example, $C_{\rm gc} - U_{\rm sw} > 0$ in experiments with $\Delta = 3/4$ and $\epsilon \gtrsim 0.5$. In these experiments, solitary waves are generated in the form of hump-shaped waves on the shallow layer in the ambient fluid. Thus, similar to the observations of Rottman & Simpson (1989) who studied bottom-propagating gravity currents in a two-layer ambient, we find that solitary waves result when the gravity current propagates at supercritical speeds relative to the ambient interfacial wave speed.

Figure 16(b) plots the relative difference $C_{\rm wv} - U_{\rm sw}$ as a function of the difference $C_{\rm gc} - U_{\rm sw}$. The diagonal line in this plot indicates values where $C_{\rm wv} = C_{\rm gc}$. In all cases, we find the leading wave speed is faster than the gravity current speed by

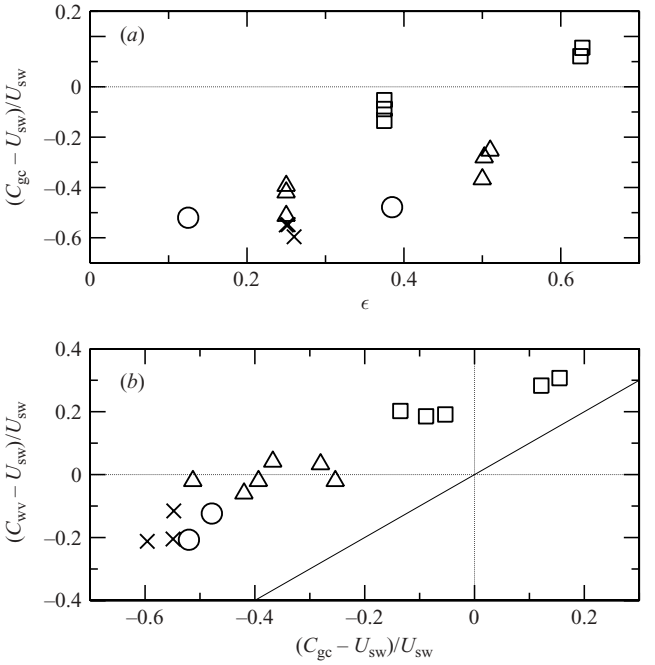

FIGURE 16. (*a*) Speed of the intrusion head, C_{gc}, relative to theoretical shallow-water wave speed U_{sw} and plotted against ϵ. (*b*) Speed of the leading interfacial wave, C_{wv}, relative to U_{sw} and plotted against the relative speed of the intrusion head. In both plots, symbols correspond to experiments with $h_T = 20\,\text{cm}$, $\sigma = 0.02$ and Δ equal to 3/4 (open square), 1/2 (open triangle), 1/4 (open circle) and 0 (cross). Points are plotted only in experiments in which interfacial waves have resolvable amplitudes. Note, interfacial wave amplitudes are negligible in experiments with $\epsilon = 0$.

approximately $0.3U_{sw}$ when $C_{wv} < U_{sw}$. The difference is smaller when $C_{wv} > U_{sw}$, corresponding to the solitary wave regime.

The analysis of leading interfacial wave amplitudes is shown in figure 17. Figure 17(*a*) shows that the measured wave amplitude A_{wv} relative to the shallow-water depth h_{sw} increases approximately linearly with the normalized gravity current speed after the speed passes a threshold. Below this threshold, the amplitudes are too small to be measured within pixel-scale resolution. Specifically, interfacial waves are observed to have significant amplitude once C_{gc} is larger than approximately 30% of the theoretical shallow-water speed U_{sw}. Experiments in which the ratio A_{wv}/h_{sw} exceeds unity correspond to those where the wave speed C_{wv} is observed to be faster than U_{sw}.

These results thereby give us an empirical prediction for the occurrence of significant leading interfacial waves. They further provide a consistent picture of the transition from linear (undulating) interfacial waves to solitary (hump-shaped) waves as the wave amplitude, A_{wv}, and speed, C_{wv}, become greater than h_{sw} and U_{sw}, respectively.

Finally, figure 17(*b*) shows that, although there is some scatter in the data, the horizontal extent of the leading interfacial wave, as represented by the equivalent wavelength λ, is set approximately by the value of h_{sw}. Typically, we find $\lambda/h_{sw} = 6.5 \pm 2$ independent of the amplitude or speed of the wave.

Taken together, figures 16(*b*) and 17(*b*) show that the wave speed and extent are primarily controlled, respectively, by the gravity current speed and the depth of the

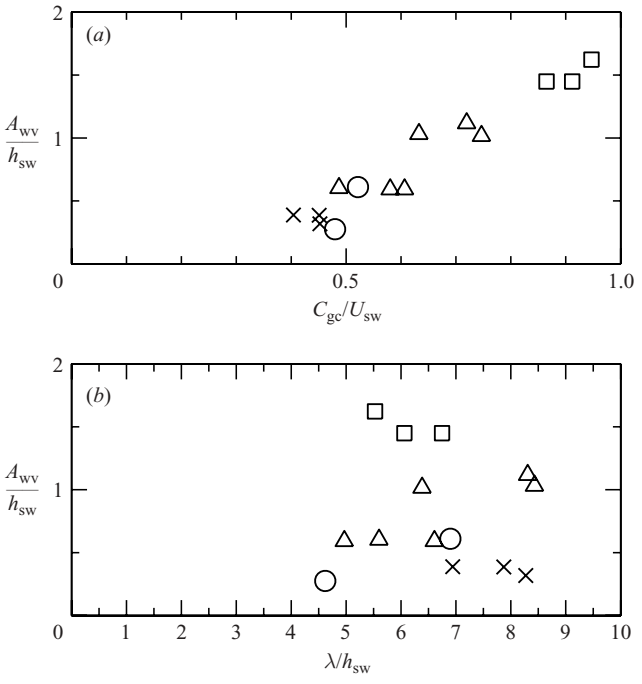

FIGURE 17. (*a*) Amplitude of leading interfacial wave, A_{wv}, normalized by equivalent shallow-water depth h_{sw} and plotted against intrusion speed normalized by shallow-water speed. (*b*) A_{wv}/h_{sw} plotted against the horizontal extent of the wave λ normalized by h_{sw}. In both plots, symbols correspond to experiments with $h_T = 20\,\text{cm}$, $\sigma = 0.02$ and symbols are drawn as in figure 16.

shallow layer, as we would anticipate from scaling arguments. Figure 17(*a*) shows that wave amplitude is controlled by the gravity current speed, implying that energetic, not geometrical, arguments are required to explain the mechanism for wave generation.

Elaborating upon this hypothesis, recall that the mean energy associated with shallow-water waves increases as the square of the wave amplitude, A_{wv}, and the kinetic energy per unit length of the intrusion is proportional to the square of its propagation speed C_{gc}. Thus, once a threshold is passed ($C_{gc} \gtrsim 0.3U_{sw}$), the energy imparted to the waves is proportional to the energy of the intrusion in excess of this threshold. The threshold itself is presumably determined by a transition from stable to unstable flow of the steady state. Theoretical analysis of this transition is beyond the scope of this work.

6. Discussion and conclusions

We have shown that the dependence of gravity current speeds on $\Delta \equiv (h_0 - h_1)/h_T$ is qualitatively well represented by the theory of Holyer & Huppert (1980) in circumstances where negligibly small interfacial waves are excited. Specifically, this occurs in cases for which $\epsilon = 0$ corresponding to experiments where the gravity current density is the weighted-mean average of the two-layer ambient fluid density. Quantitatively, the theory overpredicts the speed by approximately 10%, with better agreement in experiments with $\Delta = 0$.

If ϵ is different from zero, large-amplitude interfacial waves are excited and the current speed is significantly underpredicted by the exact theory. The qualitative trend in the observed behaviour is better captured by the second-order asymptotic approximation to theory, computed about $\epsilon = 0$, but extrapolated to ϵ outside the convergence bounds.

An empirical formula for the gravity current speed has been determined by computing as a function of A, the slopes, $m(A)$, and intercept, $b(A)$, of the best-fit lines through plots of C_{gc}/U_0 versus ϵ, such as those shown with corresponding sets of symbols in figure 13. The results of 68 experiments were used in this computation, giving values of $m(A)$ and $b(A)$ for $A = 1/4$, $\pm 1/2$ and $\pm 3/4$. The intercept, b, was found to be approximately constant and its average value was found. The slope, m, was found to increase with A and the best-fit line was then found to give a linear approximation for m as a function of A. Thus, we found the observed gravity current speed is given approximately by

$$C_{gc} \simeq U_{sw}\left[(0.44 \pm 0.02) + (2.0 \pm 0.2)A\epsilon\right]. \tag{6.1}$$

Here, we have used (5.1) to relate U_0 to U_{sw}.

The result (6.1) predicts that the gravity current speed is faster than the shallow-water speed, and hence is supercritical, when $A\epsilon \gtrsim 0.28$.

Likewise, the data plotted in figure 16 shows that C_{gc} increases as a function of A and ϵ. The computed coefficients in the linear approximation to C_{gc}/U_{sw} as a function of $A\epsilon$ give comparable values to those in (6.1) except with significantly larger errors because there is less data: the former points are plotted only in circumstances when large-amplitude interfacial waves are generated.

Using data, such as those shown in figure 16(*b*), we similarly compute the linear approximation to the observed phase speed of interfacial waves, C_{wv}, as a function of C_{gc} and U_{sw}. Explicitly, we find

$$\frac{C_{wv} - U_{sw}}{U_{sw}} \simeq (0.68 \pm 0.06)\frac{C_{gc} - U_{sw}}{U_{sw}} + (0.23 \pm 0.02).$$

Using (6.1), we therefore determine

$$C_{wv} \simeq U_{sw}\left[0.85(\pm 0.04) + 1.36(\pm 0.18)A\epsilon\right]. \tag{6.2}$$

This relation predicts that the wave speed is faster than the shallow-water speed (and hence must constitute a nonlinear solitary wave) when $A\epsilon \gtrsim 0.11$. Hence, this empirical formula predicts that solitary waves should appear before the gravity current speed is supercritical.

The response of the wave amplitude to the gravity current speed is determined empirically by finding the best-fit line to plots such as that shown in figure 17. Explicitly, we find

$$\begin{aligned}\frac{A_{wv}}{h_{sw}} &\simeq (2.44 \pm 0.18)\left(\frac{C_{gc}}{U_{sw}} + (-0.29 \pm 0.05)\right)\\ &\simeq 0.34(\pm 0.13) + 4.9(\pm 0.6)A\epsilon,\end{aligned} \tag{6.3}$$

which holds for $C_{gc} \gtrsim 0.29\ U_{sw}$. Here, we have used (6.1) to express the linear approximation explicitly in term of A and ϵ.

The empirical formula (6.3) must be employed with care. In the case $\epsilon = 0$, no significant interfacial waves are generated in experiments despite the fact that the formula predicts that wave amplitudes are finite even in the case $\epsilon = 0$. We must

interpret the formula as predicting wave amplitudes only in circumstances in which waves actually occur. Our experiments show this occurs for $|\epsilon|$ as small as 0.1.

Equation (6.3) gives an explicit prediction for the generation of nonlinear waves. The condition $A_{\rm wv} > h_{\rm sw}$ occurs if $\Delta\epsilon \gtrsim 0.16$. This result is consistent with the prediction above that the observed wave speed, $C_{\rm wv}$, exceeds the shallow-water speed, $U_{\rm sw}$.

These experiments have been performed only for the case of a full-depth lock-release in a two-layer ambient fluid. Wave-generation phenomena in the atmosphere and ocean would be better represented by partial-depth lock-release experiments in fluids with more complex stratification. This is the subject of ongoing research including work by Flynn & Sutherland (2004).

The experiments were performed in the Environmental and Industrial Fluid Dynamics Laboratory at the University of Alberta. This work has been supported by funding from the Natural Sciences and Engineering Research Council of Canada Discovery Grant, USRA and PGS-A programs, Alberta's iCore Scholarships and the Canadian Foundation for Climate and Atmospheric Science.

Appendix A. Shallow lower layer

Here we derive the perturbation expansion appropriate for a shallow lower layer in the Boussinesq approximation.

In the limit $H_1 \to 0$ in (2.12) and (2.13), we have

$$\epsilon(1-2\delta_0)^2(1+2\delta_0) = 0 \tag{A 1}$$

and

$$\epsilon\delta_0(1+2\delta_0)^2 = 0, \tag{A 2}$$

respectively. These are simultaneously satisfied for $\epsilon = 0$ or $\delta_0 = -1/2$.

Here, we are interested only in the latter case, which corresponds to $r_0 = 1$: no change in depth and consequently no change in speed in the upper layer upstream and downstream of the gravity current. For small H_1 we therefore expand assuming that $1 + 2\delta_0 = \beta H_1$ in which β is an order 1 parameter.

Then (2.12) and (2.13) become

$$(1-\epsilon)(1+2\delta_1)^2(1-2\delta_1) = 8\epsilon\beta \tag{A 3}$$

and

$$(1-\epsilon)\delta_1(1-2\delta_1)^2 = -2\epsilon\beta^2, \tag{A 4}$$

respectively.

Note that if $\epsilon \sim O(1)$ in these equations, then $\beta \sim O(1-2\delta_1)$. Hence, $\delta_1 \to 0$ as $H_1 \to 0$ and $\epsilon \simeq 1$. We cannot have $\epsilon \simeq 0$ in (A 3) and (A 4) because these equations would then simultaneously imply that $1 - 2\delta_1 \sim O(\epsilon)$ and $1 - 2\delta_1 \sim O(\epsilon^{1/2})$.

We proceed to eliminate β in (A 3) and (A 4) under the implicit assumption that $0 \ll |\epsilon| \leqslant 1$.

After some algebra we obtain $(1-\epsilon)r_1^4/\epsilon + 2r_1 - 1 = 0$, in which we have substituted $\delta_1 = r_1 - 1/2$. This equation, which implicitly defines r_1 is the result given by (2.19).

REFERENCES

Benjamin, T. B. 1968 Gravity currents and related phenomena. *J. Fluid Mech.* **31**, 209–248.

Britter, R. E. & Simpson, J. E. 1981 A note on the structure of the head of an intrusive gravity current. *J. Fluid Mech.* **112**, 459–466.

Christie, D. R. 1992 The Morning Glory of the Gulf of Carpentaria: a paradigm for non-linear waves in the lower atmosphere. *Austral. Met. Mag.* **41**, 21–60.

Clarke, J. C. 1998 Picture of the month: an atmospheric undular bore along the Texas coast. *Mon. Weather Rev.* **126**, 1098–1100.

Clarke, J. C., Smith, R. K. & Reid, D. G. 1981 The Morning Glory of the Gulf of Carpentaria: An atmospheric undular bore. *Mon. Weather Rev.* **109**, 1726–1750.

Clarke, R. H. 1984 Colliding sea-breezes and the creation of internal atmospheric bore waves: two-dimensional numerical studies. *Austral. Met. Mag.* **31**, 207–226.

Dalziel, S. B. 1992 Decay of rotating turbulence: some particle tracking experiments. *Appl. Sci. Res.* **49**, 217–244.

Faust, K. M. & Plate, E. J. 1984 Experimental investigation of intrusive gravity currents entering stably stratified fluids. *J. Hydraul. Res.* **22**, 315–325.

Flynn, M. R. & Sutherland, B. R. 2004 Interfacial gravity currents and internal gravity wave generation in continuously stratified fluids. *J. Fluid Mech.* **514**, 355–383.

Gill, A. E. 1982 *Atmosphere–Ocean dynamics.* Academic.

Haase, S. & Smith, R. K. 1984 Morning Glory wave clouds in Oklahoma: a case study. *Mon. Weather Rev.* **112**, 2078–2089.

Hacker, J., Linden, P. F. & Dalziel, S. B. 1996 Mixing in lock-release gravity currents. *Dyn. Atmos. Oceans* **24**, 183–195.

Härtel, C., Meiburg, E. & Necker, F. 2000 Analysis and direct numerical simulation of the flow at a gravity-current head. Part 1. Flow topology and front speed for slip and no-slip boundaries. *J. Fluid Mech.* **418**, 189–212.

Holyer, J. Y. & Huppert, H. E. 1980 Gravity currents entering a two-layer fluid. *J. Fluid. Mech.* **100**, 739–767.

von Kármán, T. 1940 The engineer grapples with nonlinear problems. *Bull. Am. Math. Soc.* **46**, 615–683.

Keulegan, G. H. 1957 An experimental study of the motion of saline water from locks into fresh water channels. Tech. Rep. 5168, Natl Bur. Stand.

Lowe, R. J., Linden, P. F. & Rottman, J. W. 2002 A laboratory study of the velocity structure in an intrusive gravity current. *J. Fluid Mech.* **456**, 33–48.

Mehta, A., Sutherland, B. R. & Kyba, P. J. 2002 Interfacial gravity currents: Part II – wave excitation. *Phys. Fluids* **14**, 3558–3569.

Menhofer, A., Smith, R. K., Reeder, M. J. & Christie, D. R. 1997 'Morning-Glory' disturbances and the environment in which they propagate. *J. Atmos. Sci.* **54**, 1712–1725.

Noonan, J. A. & Smith, R. K. 1985 Linear and weakly nonlinear internal wave theories applied to 'Morning Glory' waves. *Geophys. Astrophys. Fluid Dyn.* **33**, 123–143.

Noonan, J. A. & Smith, R. K. 1986 Sea breeze circulations over Cape York Peninsula and the generation of Gulf of Carpentaria cloudlike disturbances. *J. Atmos. Sci.* **43**, 1679–1695.

de Rooij, F., Linden, P. F. & Dalziel, S. B. 1999 Saline and particle-driven interfacial intrusions. *J. Fluid Mech.* **389**, 303–334.

Rottman, J. W. & Simpson, J. E. 1983 Gravity currents produced by instantaneous releases of a heavy fluid in a rectangular channel. *J. Fluid Mech.* **135**, 95–110.

Rottman, J. W. & Simpson, J. E. 1989 The formation of internal bores in the atmosphere: a laboratory model. *Q. J. R. Met. Soc.* **115**, 941–963.

Simpson, J. E. 1997 *Gravity Currents*, 2nd edn. Cambridge University Press.

Simpson, J. E. & Britter, R. E. 1979 The dynamics of the head of a gravity current advancing over a horizontal surface. *J. Fluid Mech.* **94**, 477–495.

Simpson, J. E., Mansfield, D. A. & Milford, J. R. 1977 Inland penetration of seabreeze fronts. *Q. J. R. Met. Soc.* **103**, 47–76.

Smith, R. K., Crook, N. & Roff, G. 1982 The Morning Glory: an extraordinary atmospheric undular bore. *Q. J. R. Met. Soc.* **108**, 937–956.

Sutherland, B. R. 2002 Interfacial gravity currents. I. Mixing and entrainment. *Phys. Fluids* **14**, 2244–2254.